Friction Between Steel and a Confined Inert Material Representative of Explosives Under Severe Loadings

Bastien Durand, Franck Delvare, Patrice Bailly, Didier Picart

Friction between steel and a confined inert material representative of explosives under severe loadings

Bastien Durand[1,2], Franck Delvare[3], Patrice Bailly[1] and Didier Picart[2]

[1]ENSI Bourges, Laboratoire PRISME, F-18020 Bourges, France, bastien.durand@ensi-bourges.fr

[2]CEA, DAM, Le Ripault, F-37260 Monts, France

[3]Université de Caen Basse-Normandie, UMR 6139 Laboratoire N. Oresme, F-14032 Caen, France

Abstract: The ignition of a confined explosive submitted to an impact strongly depends on the friction conditions between the explosive and the confinement material (generally steel). A test has been developed to study the friction between steel and a material mechanically representative of an explosive. The scope of interest is that of high pressures and high relative velocities (respectively 20 MPa and 10 m/s). The friction device consists of making a cylinder, formed of the material, slide through a steel tube. Axial prestress enabling the steel-material contact stress to be generated is performed by means of a screw-nut system. This confinement state avoids any fracture of the material from occurring throughout the test. Two kinds of tests are carried out: low-velocity (around 1 mm/min) and high-velocity (around 10 m/s). The relative displacement is obtained using a testing machine during the low-velocity tests, and thanks to a Hopkinson bars system during the high-velocity tests. Examination of the measurements obtained during high-velocity tests shows that a workable steady state of equilibrium has been reached. As the interface stresses cannot be measured, the friction coefficient must be determined using indirect data: force measurements obtained from the

machine or from the Hopkinson bars and strain measurements made on the exterior of the tube. The procedure to identify the steel-material friction coefficient from these measurements entails analytical modelling and finite element simulations of the mechanical behaviour of the tube-specimen assembly. The friction coefficient identified during the high-velocity tests is far higher than the coefficient identified during the low-velocity tests.

Keywords: friction, confinement, Split Hopkinson Pressure Bars, identification

1 Introduction

Solid explosives are materials able to quickly release energy under excessive loadings. Our study focuses more particularly on cases of so-called "low energy" impacts (below the shock-to-detonation threshold, which corresponds to impact velocities of some tens to hundreds of metres per second). Different experimental configurations are able to reproduce this situation [1]. One of the most commonly used is the "Steven test" [2], [3]. This consists of launching projectiles of a few hundred grams, at a velocity of some tens to hundreds of metres per second, which impact targets composed of a steel/explosive/steel assembly (Figure 1). Predicting the ignition of the explosive during this type of impact is based on numerical simulations [4].

However, prerequisite to such predictions is a deep and full awareness of the friction conditions at the explosive-steel interface. Indeed, numerical analysis shows that the time of ignition and the location of the ignition point in the target is highly influenced by the kinetic friction coefficient magnitude [5], [6], [7].

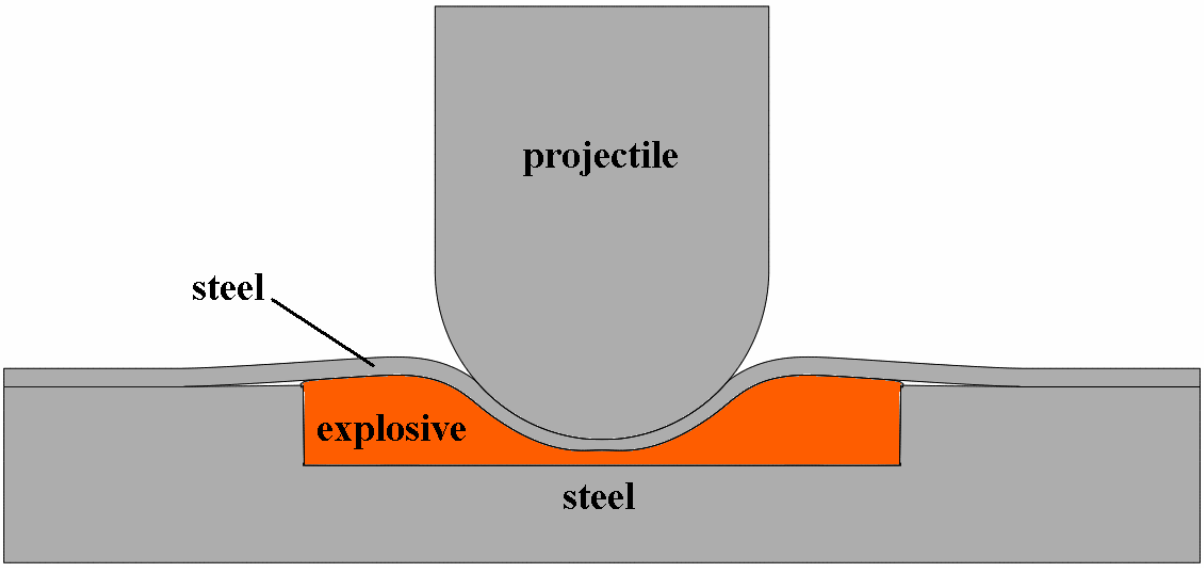

Figure 1**:** Diagram of the impact of a projectile on a target composed of a thin front plate (crushed upon impact), a disk of explosive and a thick rear plate. The diameter of the explosive disk is 99.5 mm and its height is 13 mm.

The purpose of our study is thus to develop an experimental procedure enabling the friction coefficient between an explosive and a steel to be identified under loadings generated by “low energy” impacts. This range is that of high contact pressures (several tens of MPa) combined with high sliding velocities (10 m/s). Few set-ups satisfy the pressure and velocity requirements set in this study: tribometer with explosively-driven friction [8], target-projectile assembly with oblique impact [9], [10], Hopkinson torsion bars [10], [11], [12], [13], dynamometrical ring with parallelepipedic specimen launched using a gas gun or hydraulic machine [14], [15] and, as a final possibility, the friction of a pin on a revolving disc [5]. Moreover, the desired pressures (several tens of MPa) are habitually reserved for metals [9], [10] and ceramics [12] whereas the explosives have little resistance to simple compression. This therefore requires a totally new device to be designed which enables us to confine the explosives. Indeed, a confinement configuration makes it possible to apply high pressures on an explosive sample without fracturing it. Consequently, the decision was made to design a

tubular test chamber to act as a confinement for the explosive. For safety reasons, specimens made of an inert material mechanically representative of explosives are used to carry out our tests. A pressure of the order of 10 MPa is firstly imposed at the specimen - tube interface. Then, the friction characterisation test consists of forcing the specimen to slide in the tube. The advantage of this device lies in that it may be used with a classical test machine for tests at low sliding velocities (around 1 mm/min) or can be mounted on a dynamic test bench of the Hopkinson bar type to reach high sliding velocities (around 10 m/s).

In section 2, the description of the experimental set-up is followed by a presentation of the low-velocity and high-velocity tests. The raw results are discussed, which demonstrate the interest in performing the study at high sliding velocities. In section 3, the issue of the establishment of a procedure to identify the friction is raised, such procedure being based on analytical and numerical models. The test has to be modelled since there is no way to directly measure the stresses on the sliding interfaces. Two kinds of model are proposed: an analytical one similar to the Janssen's one [16] and a numerical one using the finite element method. In section 4, the limits of the experimental device and of the friction identification procedure are discussed.

2 Experimental configurations

2.1 The inert material which is a mechanical equivalent of explosives

An equivalent inert material, denoted I1 and largely described in [17], was used for safety reasons. Its mechanical properties are known and are relatively similar to those of explosives. The Young's modulus E is 2 GPa and the Poisson's ratio ν is 0.4. The non-elastic

behaviour has been studied by carrying out triaxial compression tests. Under compressive loading, the material is able to flow when its plasticity threshold has been attained (here the maximal constraints obtained using triaxial tests are assimilated to a plasticity threshold in order to simplify the behaviour model). The plasticity flow threshold thus identified is defined by a Drucker-Prager criterion [17]:

(1) $\sigma_{eq} + \alpha P < C$

where P is the hydrostatic pressure and σ_{eq} the Von Mises equivalent stress.

As the identified behaviour is assumed to be perfectly plastic [17], the plasticity flow is defined by:

(2) $\sigma_{eq} + \alpha P = C$

The model's parameters have been identified: C = 25 MPa and α = 0.63.

According to relation (2), in the case of a simple compression loading, the maximum axial stress is only 31 MPa. The I1 specimen has therefore to be confined to reach pressures of several tens of MPa without fracturing it (the material cannot flow indefinitely).

2.2 Friction test cell enabling confinement

One way of confining a material is to enclose it in a ring [17], [18]. The idea retained is to slide a specimen of our material into a steel tube. The tube thus acts both as a sliding surface and a confining ring (Figure 2). The inner wall of the steel tube was reamed and the

specimen was turned on a sliding lathe. Both have a weak surface roughness representative of the roughness of pyrotechnic structures such as the Steven-test (Figure 1). The normal pressure at the tube-specimen interface is generated by a screw-nut system (Figure 2). The tightening of this system creates an axial prestress and as the specimen is constrained in the tube, it induces the normal pressure by Poisson effect. The relative displacement of the specimen in the tube, and thus, the tangential stress linked to the friction, is then obtained using a classical test machine for the low-velocity tests (around 1 mm/min) or by using Hopkinson bars (Figure 3) for the high-velocity tests (around 10 m/s). Thus, there are no extra effects due to radial inertia. The stresses and the sliding velocity at the interface are deduced from measurements performed by a circumferential strain gauge bonded to the external face of the tube and from measurements of forces and velocities collected by the machine or the bar system.

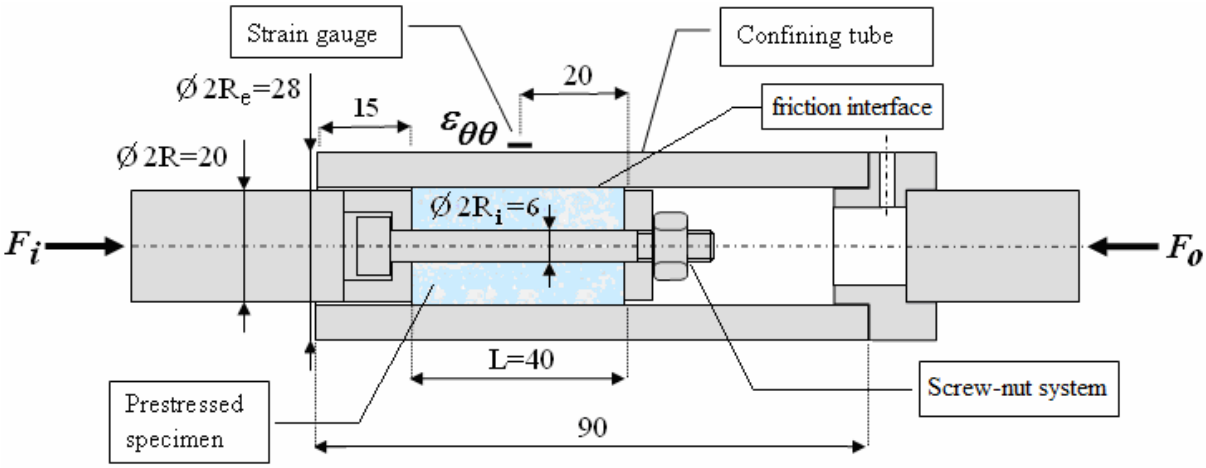

Figure 2**:** Diagram of the test cell constituted by a steel confinement and a pre-stressed specimen of the inert material (dimensions in mm).

R_e = 14 mm (external radius of the confining tube)

R = 10 mm (internal radius of the confining tube and external radius of the specimen)

R_i = 3 mm (internal radius of the specimen and radius of the screw)

L = 40 mm (length of the specimen)

F_i: force applied to the input end of the cell

F_o: force applied to the output end of the cell

$\varepsilon_{\theta\theta}$: circumferential strain measured by the gauge bonded to the external face of the tube

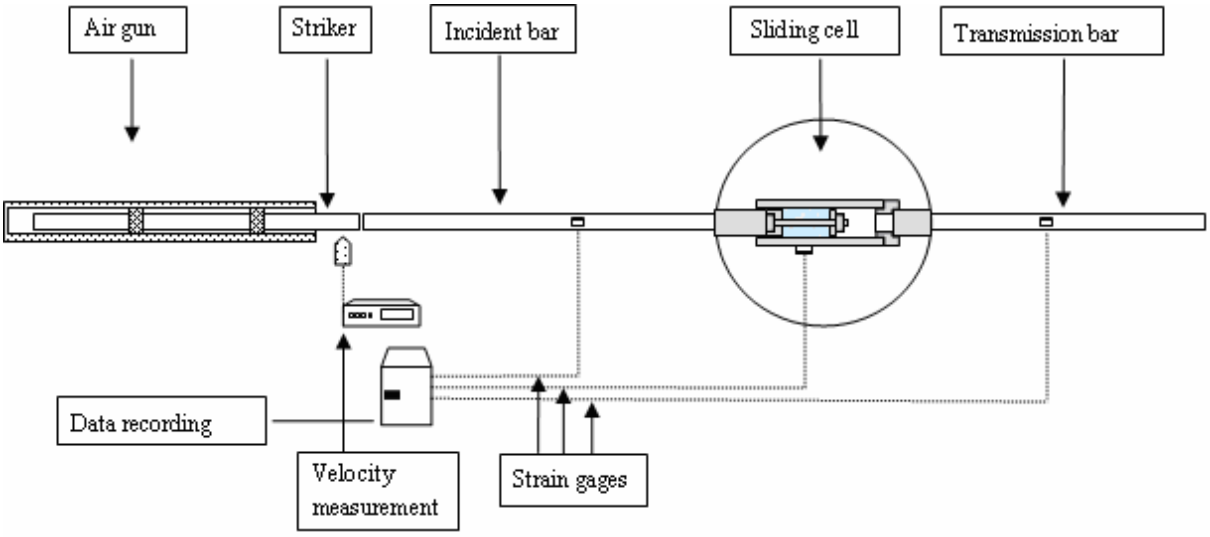

Figure 3**:** Hopkinson bar device with confinement and sliding cell.

Striker length: 1.2 m

Incident bar length: 3 m

Transmission bar length: 2 m

Bar and striker diameters: 20 mm

2.3 Low-velocity tests

A series of low-velocity tests was performed by positioning the test cell onto a classical test machine. The speed of the machine is set at 1 mm/min. Different values for the normal contact pressure were obtained by modifying the prestress due to the tightening of the screw-nut system (Figure 2). Since the device is in equilibrium during these low-velocity

tests, the forces F_i and F_o (Figure 2) are equal and denoted F. They correspond to the friction force.

Figure 4 gives, for two different values of $\varepsilon_{\theta\theta}$ (due to the pre-tightening of the screw-nut system), the evolution of F as a function of the displacement of the cross-piece Δ. These evolutions can be split into two phases: a first sticking phase during which the friction force increases until reaching a peak; then a second phase corresponding to the sliding during which the friction force remains constant. Relative motion does not occur everywhere along the interface during the first phase, which thus corresponds to the static friction; whereas relative motion occurs everywhere during the second phase, which thus corresponds to the kinetic friction. The curve forms a peak as the static friction coefficient is slightly higher than the kinetic friction coefficient. Only the second phase of the test, during which the sliding and the stress and strain states of the material specimen are assumed to be steady, is exploited.

A mean friction stress τ_{mean} can be calculated during the sliding phase as the length L (L = 40 mm) and external radius R (R = 10 mm) of the specimen are known (Figure 5).

$$\tau_{mean} = \frac{F}{2\pi RL} \quad (3)$$

An indicative value of the pressure level at the interface p_{ind} is obtained using the strain measurement $\varepsilon_{\theta\theta}$ given during the steady phase by the circumferential strain gauge bonded on the tube (Figure 2):

(4) $$p_{ind} = \frac{E_t\left(R_e^{\,2} - R^2\right)}{2R^2}\varepsilon_{\theta\theta}$$

where E_t is the Young's modulus of the tube (E_t = 210 GPa) and R_e its external radius (R_e = 14 mm) (Figure 2).

Indeed, if no friction occurs at the tube-specimen interface, the formula (4) gives the pressure at this interface exactly.

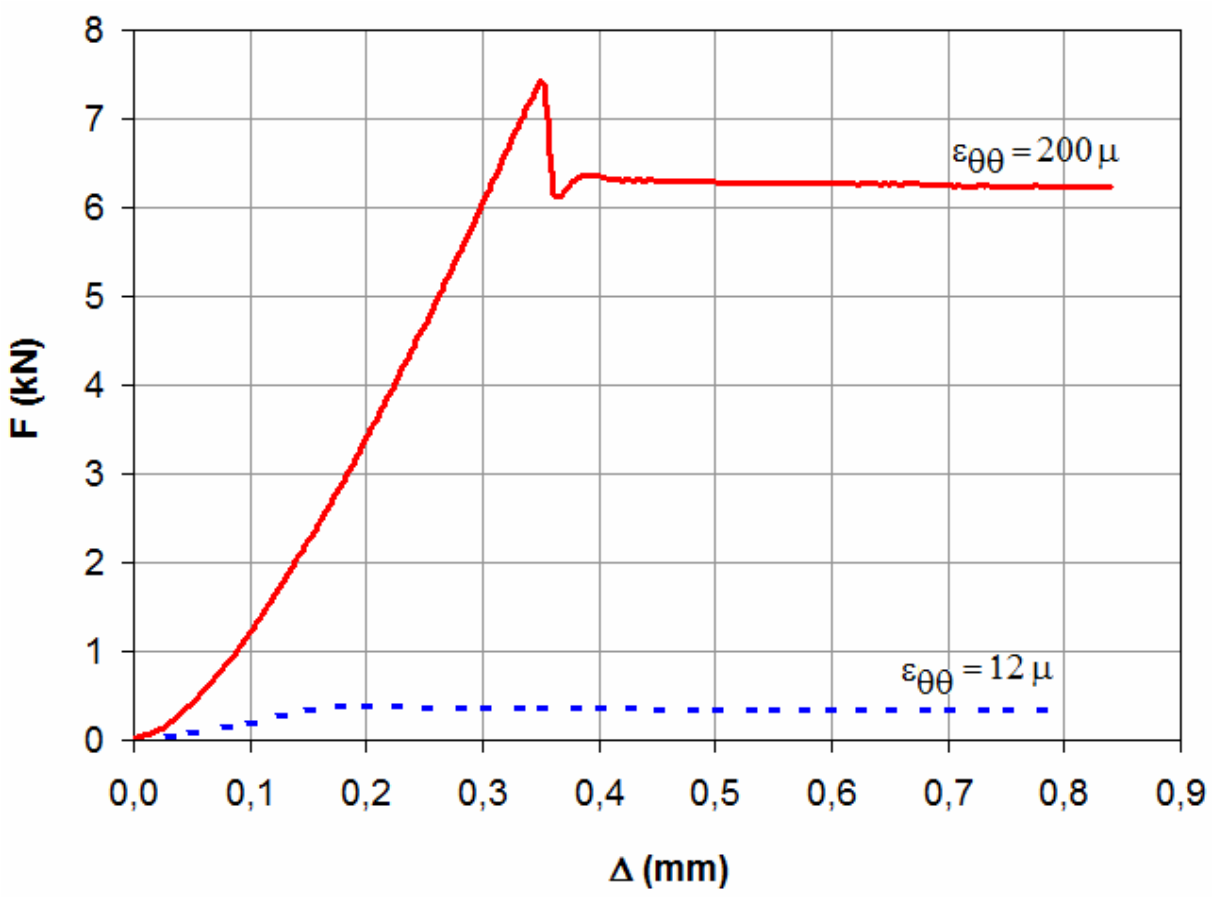

Figure 4**:** Evolutions (for the smallest and the largest values of $\varepsilon_{\theta\theta}$ (μ) due to the pre-tightening of the screw-nut system, see Figure 2) of the friction force F (kN) as a function of the displacement of the machine Δ (mm).

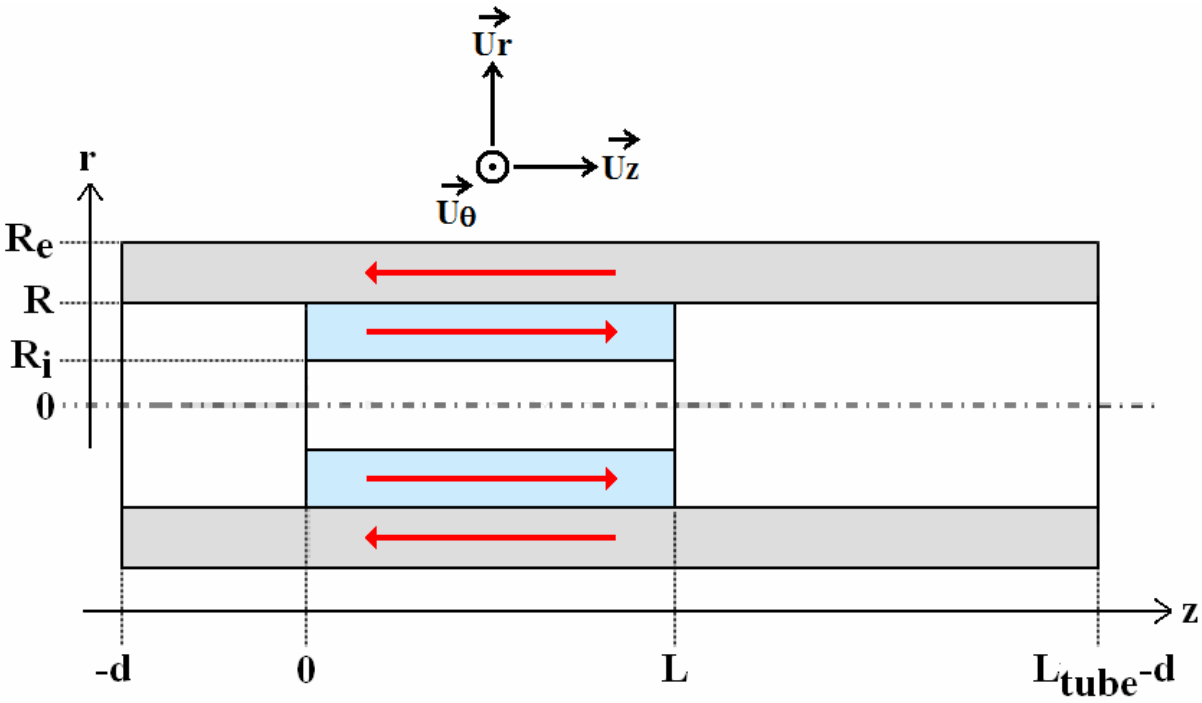

Figure 5**:** Definition of the sliding direction, of the axis $\vec{u_r}$, $\vec{u_\theta}$ and $\vec{u_z}$, and of the radial *r* and axial *z* coordinates over the tube-specimen assembly.

d = 15 mm (initial position of the specimen relatively to the tube)

L_{tube} =90 mm (length of the tube)

See Figure 2 for the other symbols.

2.4 High-velocity tests (using a Hopkinson bar apparatus)

The previously described confinement and sliding cell (section 2.2 and Figure 2) is mounted on a system of Hopkinson bars [17], [18] (Figure 3). The impact of the striker generates a compressive incident strain wave ε_i in the input bar. When this wave reaches the cell, a reflected wave ε_r appears in the input bar and a transmitted wave ε_t appears in the output bar. Longitudinal gauges are bonded on the two bars enabling the three strains ε_i, ε_r and ε_t to be determined. The bars and the striker are made of a hard stainless steel (a nickel alloy), whose yield strength is 1 GPa. The forces and velocities at the input and output ends of

the cell (section 2.2, Figure 2 and Figure 3) can be deduced from the three measured strain waves by using the following relations:

$$(5) \qquad \begin{cases} V_i = C_b\left(\varepsilon_r - \varepsilon_i\right) \\ V_o = -C_b\varepsilon_t \end{cases}$$

$$(6) \qquad \begin{cases} F_i = -S_b E_b\left(\varepsilon_i + \varepsilon_r\right) \\ F_o = -S_b E_b\varepsilon_t \end{cases}$$

V_i and V_o respectively designate the velocities at the input and output ends of the cell. S_b and E_b represent respectively the cross-section of the bars and the Young's modulus of the bars (E_b = 140 GPa), and C_b the celerity of the longitudinal waves through the bars. ε_i and ε_r correspond here to the strains to be measured at the input bar - cell interface (which corresponds to the left hand end of the cell, see Figure 2 and Figure 3) and ε_t corresponds to the strain to be measured at the output bar - cell interface (which corresponds to the right hand end of the cell).

A phase of quasi-equilibrium of the forces applied to the cell enables a simple exploitation of the test. This quasi-equilibrium state is verified when the forces are identical at the two ends of the cell:

$$(7) \qquad F_i \approx F_o$$

When this quasi-equilibrium state becomes steady, the sliding velocity V at the interface between the steel confinement tube and the specimen I1 is estimated by:

(8) $V = V_i - V_o$

It is this phase which constitutes the useful part of the test.

Figure 6 gives the raw signals recorded by the strain gauges for two pre-tightening values. The first non-zero values (positive) appearing on the signal given by the gauge bonded to the input bar (on the red curve) correspond to ε_i and the second (negative) to ε_r. The following non-zero values appearing on the signals given by the gauges bonded to the output bar (green curve) and on the tube (blue curve) respectively correspond to ε_t and to $\varepsilon_{\theta\theta}$ (section 2.2). The appearance of a steady phase can be observed on all the signals. It should be noted that the gain (the raw signal over strain ratio) for the gauges bonded to the bars has been set to a value of 1,040 V whereas that of the gauge bonded to the tube has been set to a value of 6,240 V. Furthermore, the signals of the gauges bonded to the bars have been inverted.

The forces are determined by using the equations (6). Figure 7 gives the evolution of the different forces for the two pre-tightening values. Naturally, the equilibrium of the forces is not reached immediately. There is, however, a relatively long steady equilibrium state phase (approximately from 150 µs to 550 µs) characterised by the equality given by equation (7) and by constant forces and sliding velocity V (Figure 8). This corresponds to the sliding state being established over the full interface. Any mistake in the time-shifting of the waves has an effect on the estimation of the forces and velocities in the transient phase but nevertheless remains without effect upon the analysis of the steady state phase.

For two pre-tightening values, Figure 9 gives the evolution of the normal pressure and of the friction stress over time. A steady state is established after around one hundred microseconds. The signal transmitted by the gauge bonded to the tube, from which p_{ind} is calculated, can be seen to be noisy. The mean friction stress τ_{mean} is calculated from the output force F_o rather than from the input force F_i since the aim is to sidestep the problem of the timing of the incident and reflected waves:

(9) $$\tau_{mean} = \frac{F_o}{2\pi RL}$$

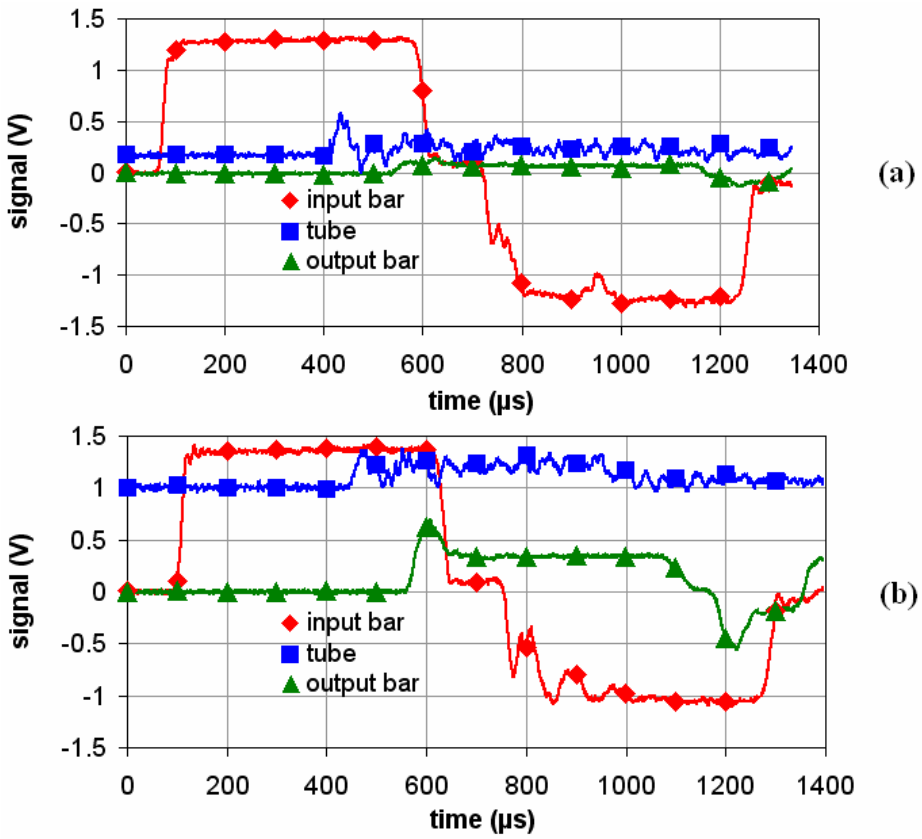

Figure 6**:** Raw signals from the strain gauges.

(a): smallest pre-tightening value

(b): largest pre-tightening value

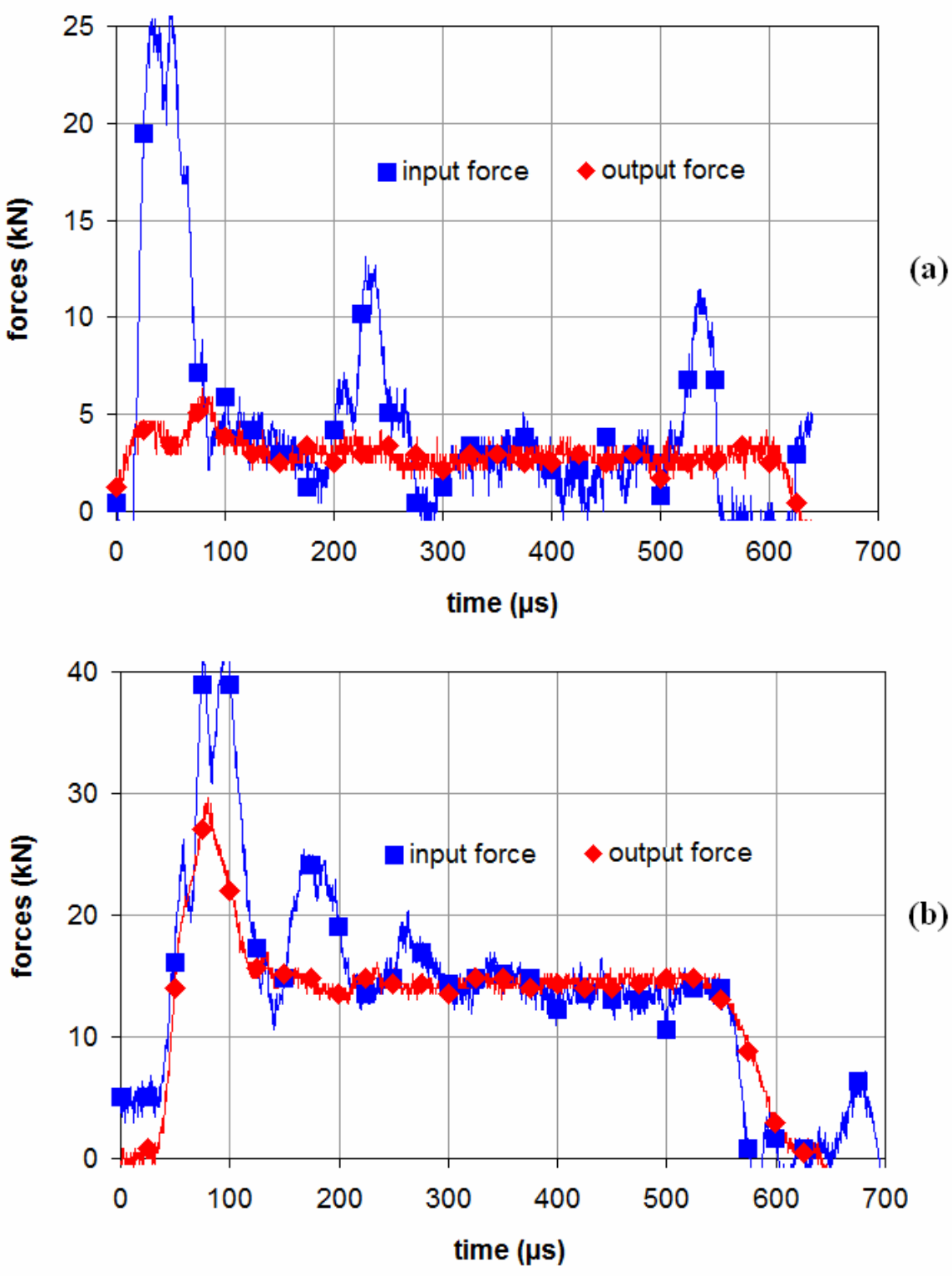

Figure 7**:** Forces F_i and F_o respectively applied to the input and output ends of the device.

(a): smallest pre-tightening value

(b): largest pre-tightening value

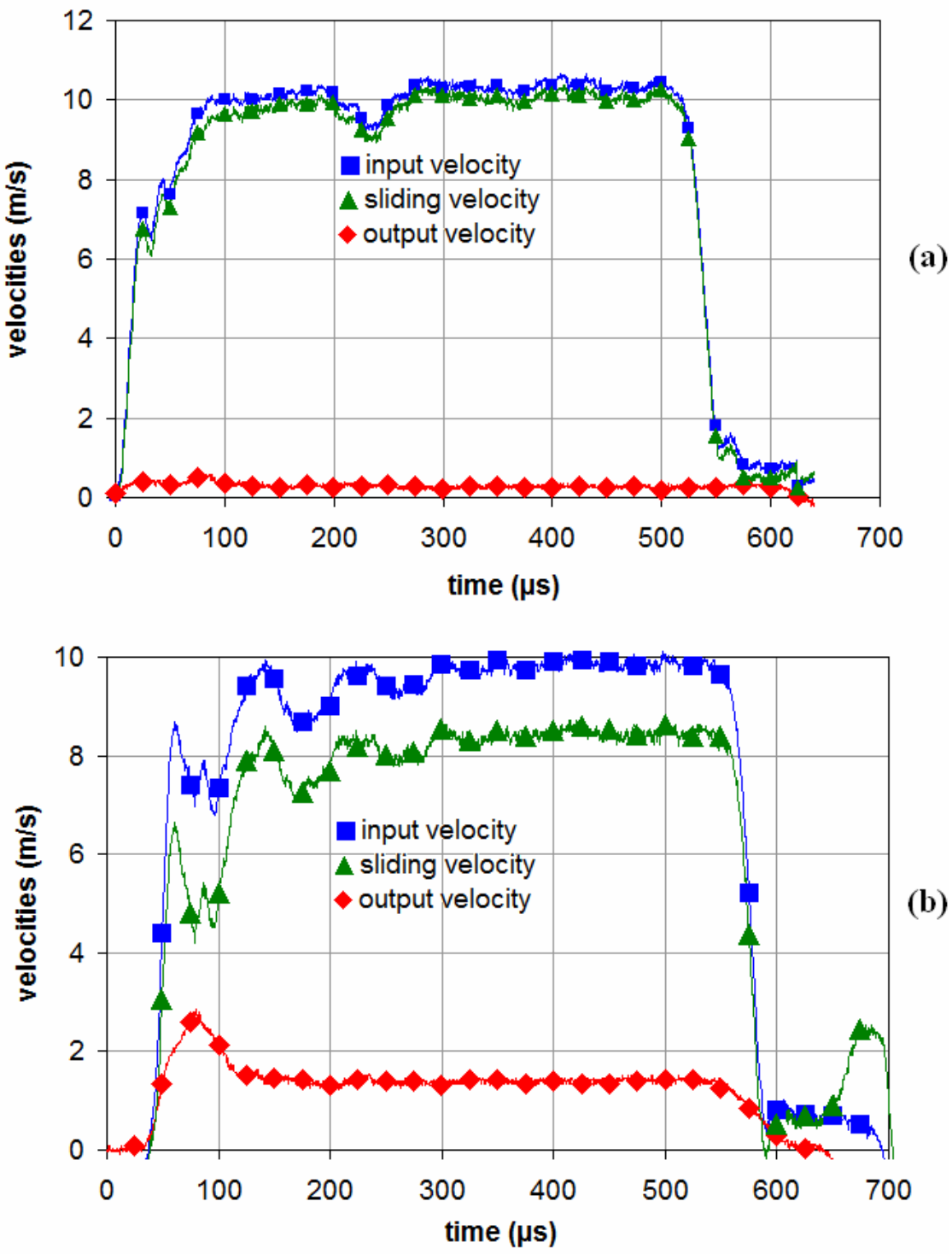

Figure 8**:** V_i, V_o and V, respectively, velocity of the input end of the cell, velocity of the output end of the cell and sliding velocity.

(a): smallest pre-tightening value

(b): largest pre-tightening value

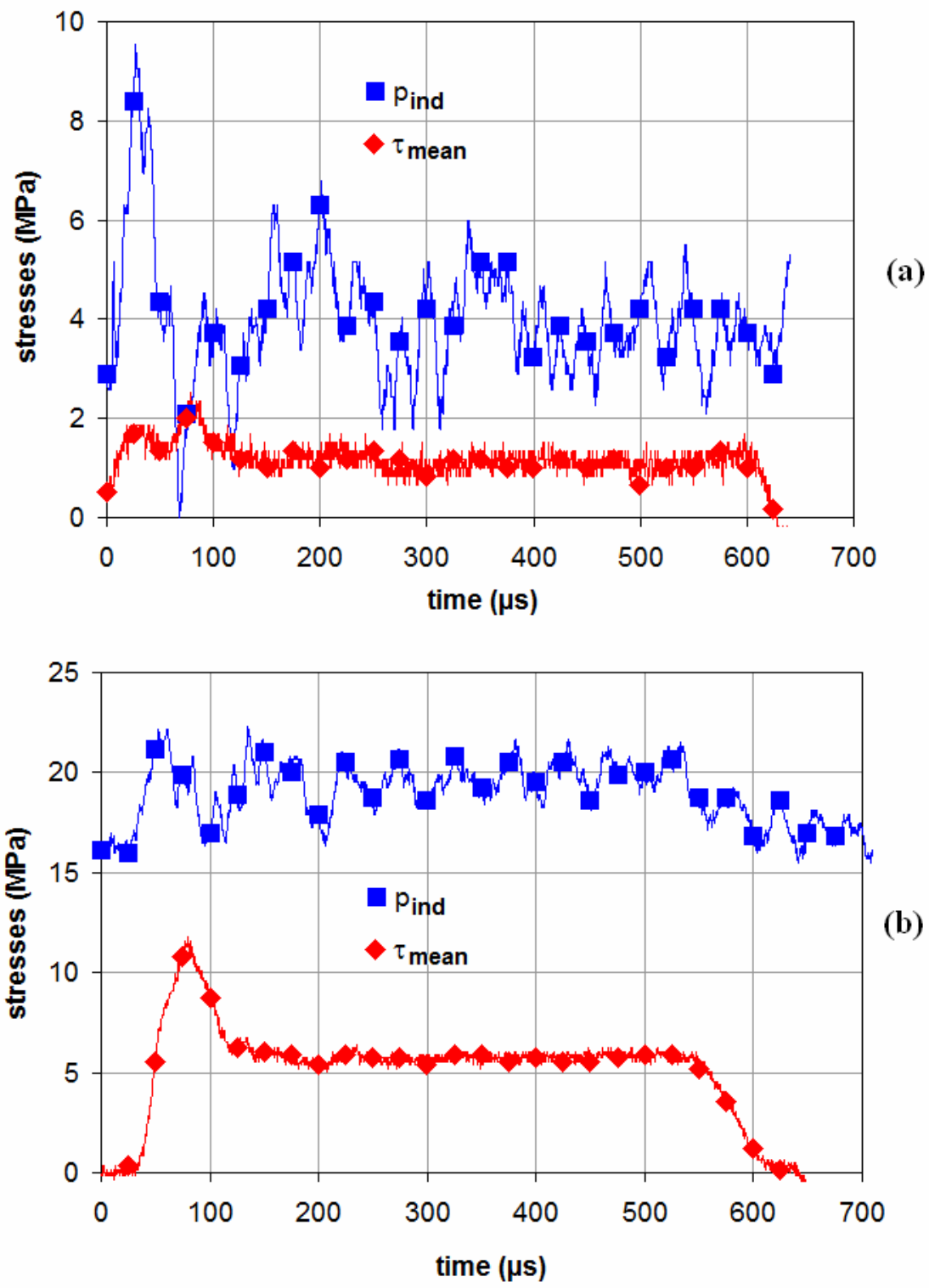

Figure 9**:** Levels of normal pressure (p_{ind}) and shear stress (τ_{mean}) at the interface during a test.

(a): smallest pre-tightening value

(b): largest pre-tightening value

2.5 Summary of experimental results

All the results are given in Figure 10. Each test is shown in the form of a dot, with the steady values of the τ_{mean} and p_{ind} stresses being plotted on the vertical and horizontal axes. The slope of the curves obtained gives an order of magnitude of the friction coefficient. Its value is 0.13 for low-velocity tests (carried out at 1 mm/min) and 0.31 for high-velocity tests (carried out at around 8-10 m/s). This latter result is consistent with that obtained by Dickson et al. for PBX 9501 [5], with a friction coefficient of around 0.3-0.5 for a velocity of 14 m/s and a pressure of 4-5 MPa. Hoffman et al. [6] performed tests similar to those of Dickson et al. [5], but at pressures largely under those in which we are interested, the results therefore cannot be compared.

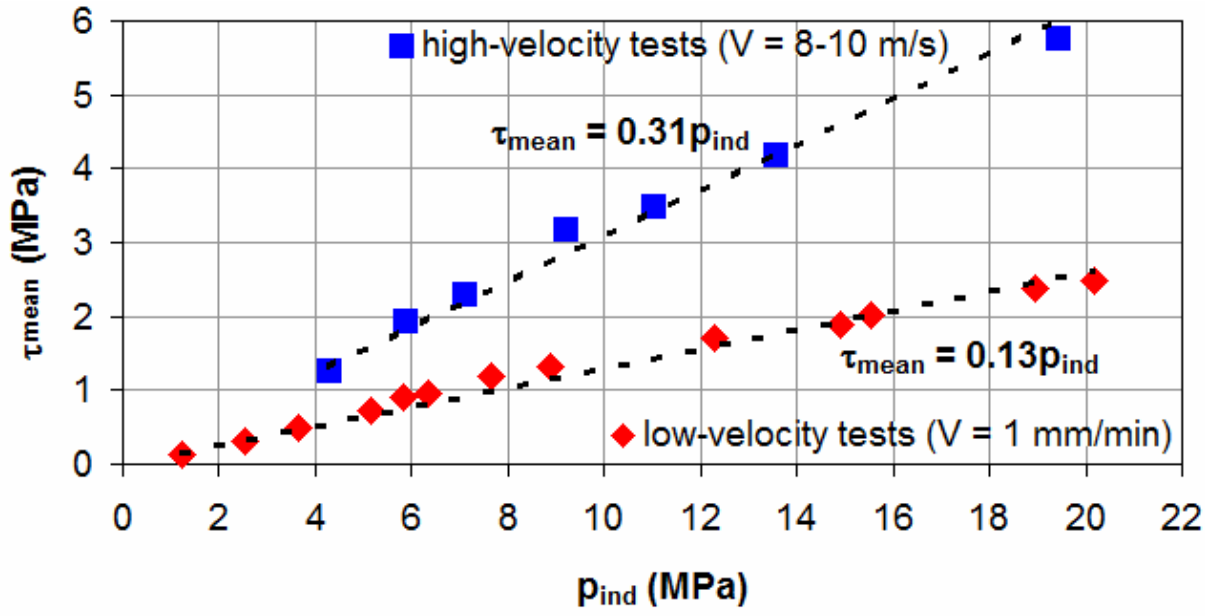

Figure 10**:** Shear stress τ_{mean} as a function of the normal stress p_{ind}. Results obtained during sliding phases of low and high velocity tests.

This study shows the feasibility of the high-velocity tests. The sensitivity of the friction to the sliding velocity emphasizes the necessity of reproducing in the test the velocities encountered in so-called "low energy" impacts (whose magnitudes are of the order of 10 m/s). Indeed, it is apparent that for the intended application (simulation of "low energy" impacts) friction conditions deduced from tests conducted at 1 mm/min may not reasonably be taken into consideration.

3 Identification of the friction coefficient

The interface stresses cannot be directly measured and the test can be exploited (and the friction coefficient identified) only if they can be estimated. One model is proposed based on an approximate solution of the elastic equilibrium of the cylinder of material I1. This simplified approach consists of considering the equilibrium of slices of elementary thickness constituting the cylinder [16]. Numerical simulations will then enable the level of approximation of this model to be judged and the assumption of an elastic behaviour will be verified too.

3.1 Analytical modelling

The stress and strain states in the I1 specimen have rotational symmetry and the stress tensor $\underline{\underline{\sigma}}$ and the strain tensor $\underline{\underline{\varepsilon}}$ are as follows:

(10) $\underline{\underline{\sigma}} = \begin{pmatrix} \sigma_{rr} & 0 & \sigma_{rz} \\ 0 & \sigma_{\theta\theta} & 0 \\ \sigma_{rz} & 0 & \sigma_{zz} \end{pmatrix}_{\vec{u_r},\vec{u_\theta},\vec{u_z}}$ and $\underline{\underline{\varepsilon}} = \begin{pmatrix} \varepsilon_{rr} & 0 & \varepsilon_{rz} \\ 0 & \varepsilon_{\theta\theta} & 0 \\ \varepsilon_{rz} & 0 & \varepsilon_{zz} \end{pmatrix}_{\vec{u_r},\vec{u_\theta},\vec{u_z}}$

The axis are defined on Figure 5.

Therefore, u_{ri}^{tube} is the initial difference in radii between the exterior of the specimen and the interior of the tube. u_{ri}^{tube} is defined such that $u_{ri}^{tube} < 0$ where there is radial clearance and $u_{ri}^{tube} > 0$ where there is radial extra thickness. Similarly, u_{ri}^{screw} is the initial difference in radii between the screw and the interior of the specimen. u_{ri}^{screw} is defined such that $u_{ri}^{screw} < 0$ where there is radial clerance and $u_{ri}^{screw} > 0$ where there is radial extra thickness (see Figure 11).

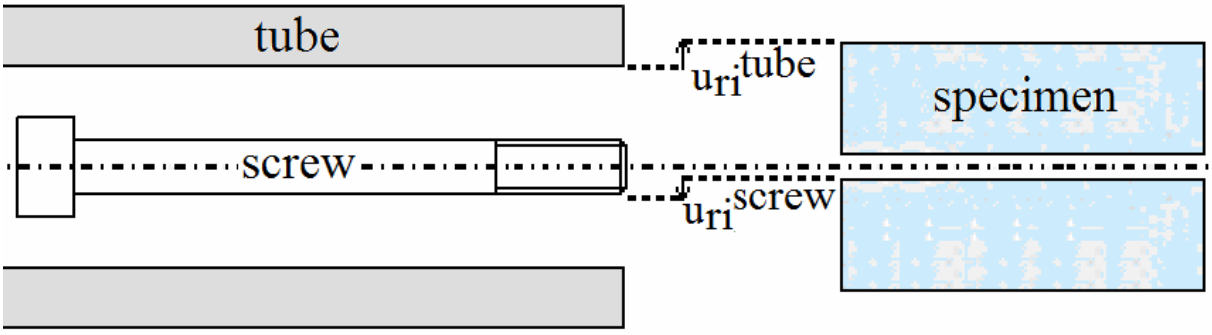

Figure 11: Definition of u_{ri}^{tube}: initial difference in radii between the exterior of the specimen and the interior of the tube and of u_{ri}^{screw}: initial difference in radii between the screw and the interior of the specimen.

The tube and the screw are assumed to be perfectly rigid. There is therefore no coupling between the behaviours of the tube, of the screw and of the specimen. If the specimen is slender enough, then ε_{rr} and σ_{rr} can be assumed to be independent of r and $\varepsilon_{\theta\theta}$ can be assumed to be linearly dependent of r:

$$(11)\quad \begin{cases} \varepsilon_{rr} = -\dfrac{u_{ri}^{\,tube} + u_{ri}^{\,screw}}{R - R_i} \\ \varepsilon_{\theta\theta}(r) = \dfrac{1}{R - R_i}\left[\dfrac{u_{ri}^{\,tube}}{R}(R_i - r) + \dfrac{u_{ri}^{\,screw}}{R_i}(R - r)\right] \end{cases}$$

where R_i is the inner radius of the specimen (R_i = 3 mm), see Figure 2. Using Hooke's law, this gives:

$$(12)\ \sigma_{zz}(r,z) = \frac{1-\nu}{\nu}\sigma_{rr}(z) + \frac{E}{\nu(1+\nu)(R-R_i)}\left[\nu\left(u_{ri}^{\,tube}\frac{r-R_i}{R} + u_{ri}^{\,screw}\frac{r-R}{R_i}\right) + u_{ri}^{\,tube} + u_{ri}^{\,screw}\right]$$

E and ν are respectively the Young's modulus and the Poisson's ratio of I1 whose numerical values are given in section 2.1.

If the friction stresses at the interface with the screw (at $r = R_i$, see Figure 2) are put aside, the elastic equilibrium of an infinitesimal slice of the specimen with a thickness dz located at z results in:

$$(13)\quad \int_{R_i}^{R} r[\sigma_{zz}(r,z) - \sigma_{zz}(r,z+dz)]dr = R\sigma_{rz}(R,z)dz$$

The friction condition is expressed as:

$$(14)\quad \sigma_{rz}(R,z) = f\sigma_{rr}(R,z) = f\sigma_{rr}(z)$$

where f is the friction coefficient at the interface with the tube (at $r = R$), see Figure 2 and Figure 5.

In this case, relation (13) becomes:

$$(15) \qquad -\int_{R_i}^{R} r\sigma_{zz,z}(r,z)dr = f\,R\sigma_{rr}(z)$$

However, according to equation (12):

$$(16) \qquad \sigma_{zz,z}(r,z) = \frac{1-\nu}{\nu}\sigma_{rr,z}(z)$$

Using the equality (15), the differential equation governing the distribution of the radial stress is obtained:

$$(17) \qquad \sigma_{rr,z}(z) = -\frac{2\nu f R}{(1-\nu)\left(R^2 - R_i^{\,2}\right)}\sigma_{rr}(z)$$

Let *p(z)* and $\tau(z)$ be the pressure and friction stresses at the interface with the tube (at *r = R)*, see Figure 2 and Figure 5:

$$(18) \qquad \begin{cases} p(z) = -\sigma_{rr}(R,z) = -\sigma_{rr}(z) > 0 \\ \tau(z) = -\sigma_{rz}(R,z) > 0 \end{cases}$$

According to relations (14) and (17), the interface stresses can be expressed as a function of τ_{mean}:

(19) $$\begin{cases} \tau(z) = \dfrac{f\beta L\,\tau_{mean}\exp\left(f\beta(L-z)\right)}{\left[\exp(f\beta L)-1\right]} \\ p(z) = \dfrac{\tau(z)}{f} \end{cases}$$

where β being defined as:

(20) $$\beta = \frac{2R\nu}{(1-\nu)\left(R^2 - R_i^{\,2}\right)}$$

Since the confinement tube is of reduced thickness, the circumferential strain along the external face of the tube $\varepsilon_{\theta\theta}(z)$ (at $r = R_e$, see Figure 5) can be estimated. For $z \in [0,L]$, the normal stresses $p(z)$ make a direct contribution to $\varepsilon_{\theta\theta}(z)$ of the form:

(21) $$\frac{2R^2}{E_t\left(R_e^{\,2} - R^2\right)}\,p(z)$$

Since the tube is blocked to the right (Figure 2), for $z \in [0,L]$, the tangential stresses $\tau(z)$ make an indirect contribution by Poisson's effect to $\varepsilon_{\theta\theta}(z)$ of the form:

(22) $$\frac{\nu_t}{E_t\pi\left(R_e^{\,2} - R^2\right)}\int_0^z 2\pi R\,\tau(\zeta)\,d\zeta$$

where ν_t is the Poisson's ratio of the tube (ν_t = 0.33).

For $z \in [0,L]$ the following formula can be deduced:

(23) $$\varepsilon_{\theta\theta}(z) = \frac{2RL\tau_{mean}\left[(\beta R - \nu_t)\exp(-f\beta z) + \nu_t\right]}{E_t\left(R_e{}^2 - R^2\right)\left[1 - \exp(-f\beta L)\right]}$$

If z_g represents the position of the strain gauge glued on the tube (Figure 2), the indicative values of the interface pressures can be expressed as:

(24) $$p_{ind} = \frac{E_t\left(R_e{}^2 - R^2\right)}{2R^2}\varepsilon_{\theta\theta}\left(z_g\right)$$

According to relation (23) this gives:

(25) $$\frac{\tau_{mean}}{p_{ind}} = \frac{R\left[1 - \exp(-f\beta L)\right]}{L\left[(\beta R - \nu_t)\exp\left(-f\beta z_g\right) + \nu_t\right]}$$

In relation (25), all the parameters are known with the exception of *f*, this relation thus enables the form of the dependence of $\frac{\tau_{mean}}{p_{ind}}$ to *f* to be estimated.

Using a first order Taylor expansion of the function *exp*, the formula (25) leads to an affine relationship between $\frac{1}{f}$ and $\frac{p_{ind}}{\tau_{mean}}$. Figure 12 shows the validity of this approximation.

This approximation enables *f* to be identified from the values of $\frac{\tau_{mean}}{p_{ind}}$ measured during the tests (Figure 10). This gives, with z_g = 20 mm, *f* = 0.14 for the low-velocity tests and *f* = 0.37 for the high-velocity tests.

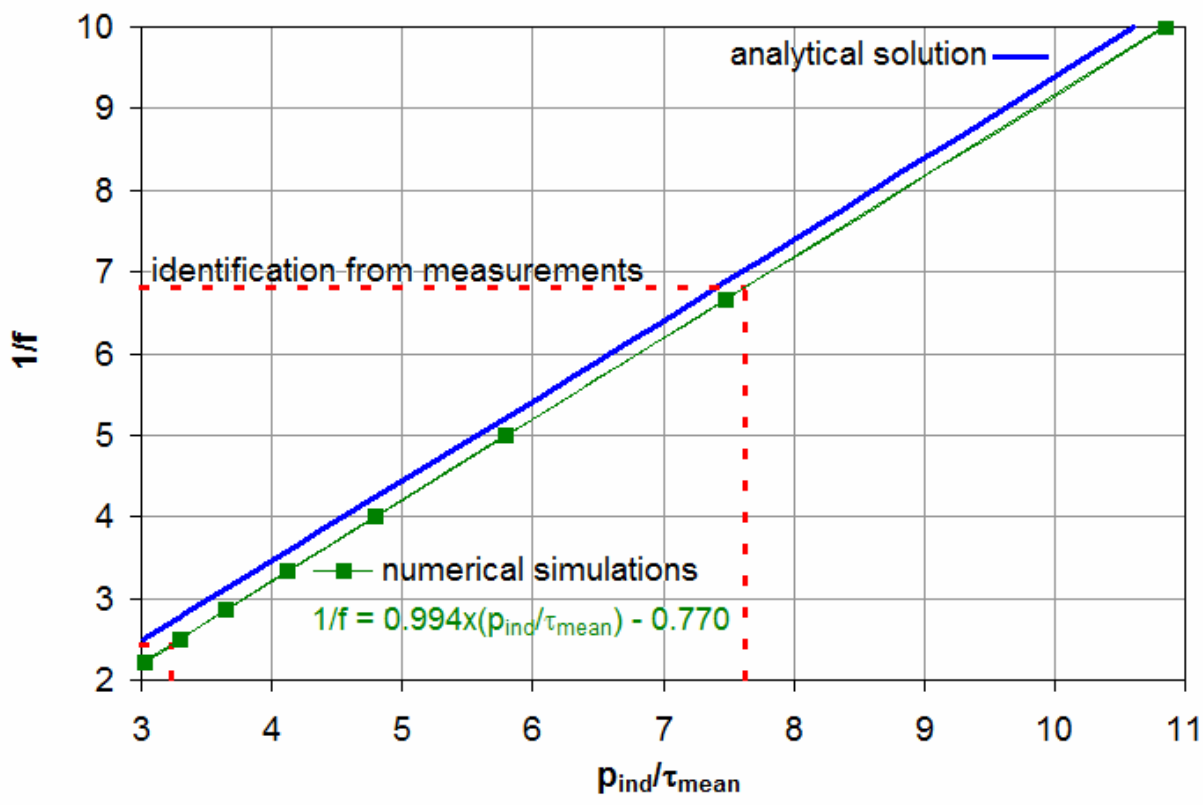

Figure 12**:** Numerical and analytical (from relation (25)) evolutions of $\frac{1}{f}$ as a function of $\frac{p_{ind}}{\tau_{mean}}$. Evolutions obtained with z_g = 20 mm.

The strain gauge is glued on the tube (Figure 2). As the specimen moves relatively to the tube, z_g (the position of the gauge relatively to the specimen) varies during the tests and initially, z_g = 20 mm (Figure 2). The *f* relative uncertainty $\frac{\Delta f}{f}$ due to the z_g uncertainty Δz_g can be deduced from relation (25) which leads to:

(26) $$\frac{\Delta f}{f} = \frac{\Delta z_g}{\left| \frac{\left[(\beta R - \nu_t)\exp(-f\beta z_g) + \nu_t\right] L \exp(-f\beta L)}{\left[1-\exp(-f\beta L)\right](\nu_t - \beta R)\exp(-f\beta z_g)} - z_g \right|}$$

In the case of the low-velocity tests, the displacement of the specimen in the tube is less than 1 mm (Figure 4) and $f = 0.14$, which leads to $\frac{\Delta f}{f} < 2\ \%$. As a result, the friction coefficient obtained with $z_g = 20$ mm can be considered to be reliable.

In the case of high-velocity tests, the sliding velocity between the specimen and the tube can reach almost 10 m/s during 500 µs (Figure 8). It leads to a relative displacement of 5 mm, which cannot be neglected relatively to the specimen length. Thus, the position of the strain gauge z_g varies from 20 mm to 15 mm. Even if the specimen remains in a stationary state (which implies that τ_{mean} remains constant), p_{ind}, which depends on z_g, increases but this variation cannot be seen on Figure 9 because of the noise. The uncertainty due the relative displacement can be taken into account by identifying f with $z_g = 15$ mm, which leads to $f = 0.45$ (whereas $z_g = 20$ mm leads to $f = 0.37$).

3.2 Finite element simulations

Numerical simulations based on the finite element method are performed using ABAQUS CAE / Standard. The computations are made in two-dimensional axisymmetric configuration with quadrangular elements having quadratic interpolation. Only the I1 specimen and the steel tube are modelled and their mechanical behaviours are assumed to be perfectly elastic (which is checked in section 4.1). They are discretized by 0.2 mm x 0.2 mm size square elements. The normal contact between both parts is defined by a direct hard contact (no interpenetration) and separation is enabled (no adhesion). The tangential contact obeys a Coulomb's law imposed by Lagrange multipliers. The test is simulated with friction coefficients f varying from 0.10 to 0.45 by step of 0.05. The presence of the screw is modelled by an imposed displacement boundary condition. The radial displacement is assumed equal to

u_{ri}^{screw} on the interface (Figure 13). The influence of the friction between screw and specimen is assumed to be negligible (no tangential stresses). The tightening of the screw-nut assembly is modelled by axial displacements imposed at the two ends of the specimen. Moreover, the specimen being pushed in the tube, a displacement is imposed on the right face of the tube (Figure 13).

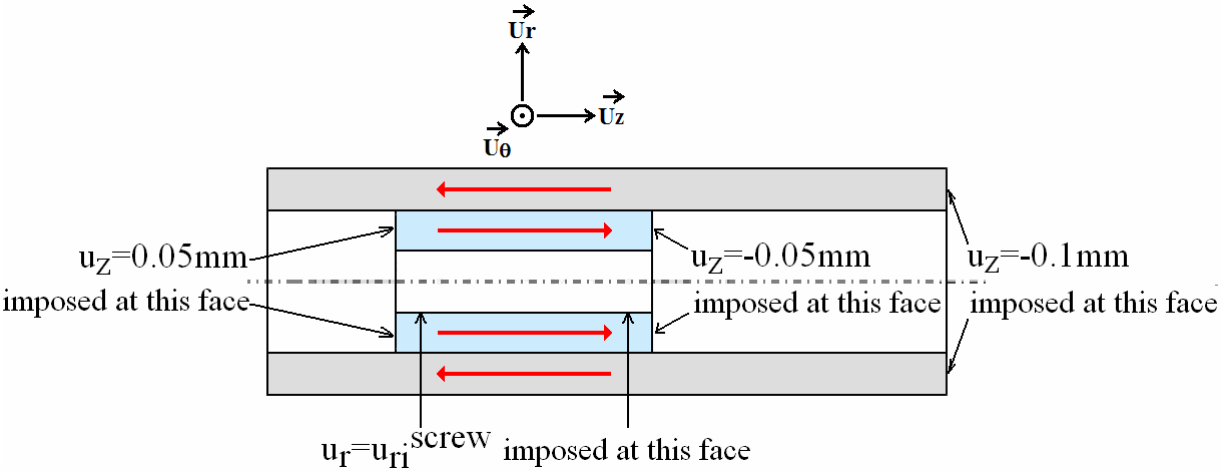

Figure 13**:** Axial and radial displacements (u_z and u_r) imposed on the tube-specimen assembly.

The numerical results presented in Figure 12 were obtained with $u_{ri}^{tube} = 0$ and $u_{ri}^{screw} = 0$. The relation between $\frac{1}{f}$ and $\frac{p_{ind}}{\tau_{mean}}$ is also approximated by means of a linear regression. Using the values of $\frac{\tau_{mean}}{p_{ind}}$ obtained experimentally (Figure 10), it can be deduced from the numerical model that $f = 0.15$ for the low-velocity tests and that $f = 0.41$ for the high velocity tests. Thus, the relative error produced by the simplified analytical model can be observed to be 3 % when determining the friction coefficient corresponding to $\frac{\tau_{mean}}{p_{ind}} = 0.13$ and 10 % when determining the friction coefficient corresponding to $\frac{\tau_{mean}}{p_{ind}} = 0.31$.

For the high-velocity tests, the uncertainty due the relative displacement is taken into account by applying a 5 mm axial displacement on the tube (Figure 13) in additional simulations (instead of 0.1 mm). f = 0.56 is identified from these simulations.

The friction coefficient thus being calculated for both types of test (low and high sliding velocities), it is possible, for each test, for the mean pressure p_{mean} at the interface to be estimated from the values of τ_{mean} obtained by measurement (Figure 10). Thus, we can check if the desired pressures have been reached. The results obtained with the friction coefficient estimated from the numerical simulations are presented in Figure 14.

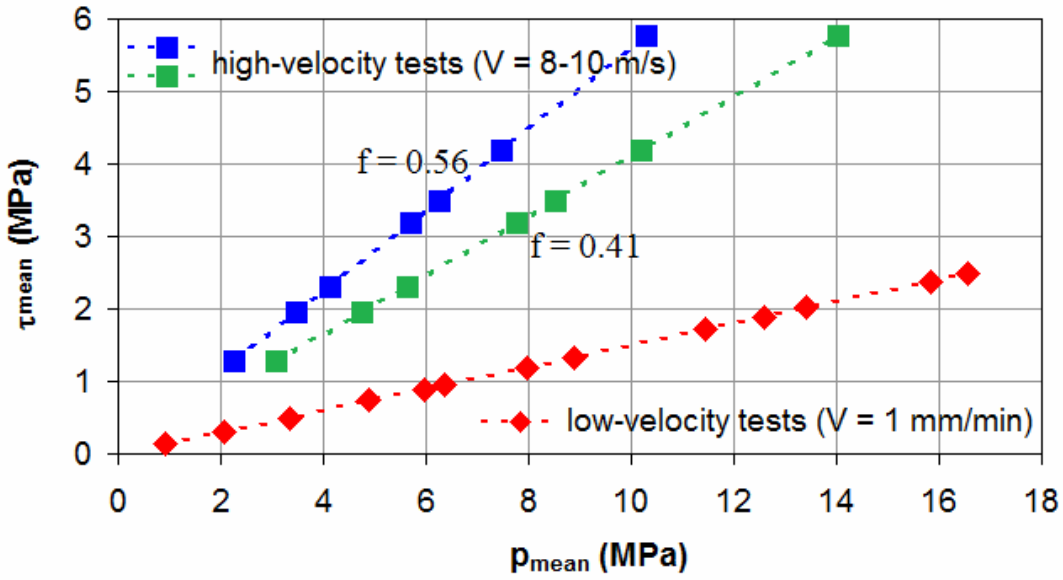

Figure 14**:** Evolution of the experimental mean friction stress τ_{mean} as a function of the mean pressure p_{mean} (calculated from the experimental mean friction stress τ_{mean} and the from the numerical friction coefficient). For the low-velocity tests, each dot corresponds to a test. For the high-velocity tests, two values of p_{mean} (corresponding respectively to f = 0.41 and f = 0.56) are calculated for each value of τ_{mean}.

According to relation (19) this gives:

$$(27) \qquad \frac{\tau(z)}{\tau_{mean}} = f\beta L \frac{\exp\left(f\beta L\left(1-\frac{z}{L}\right)\right)}{\exp(f\beta L)-1}$$

It is thus possible for the stress profiles provided by the analytical model and by the numerical simulations to be compared. Figure 15 shows that formula (19) gives results that are similar to those given by the numerical simulations although it does not allow any edge effects to be taken into account. The error produced by the analytical model is essentially due to the approximation of a reduced thickness for the confinement tube used to establish the formula (23).

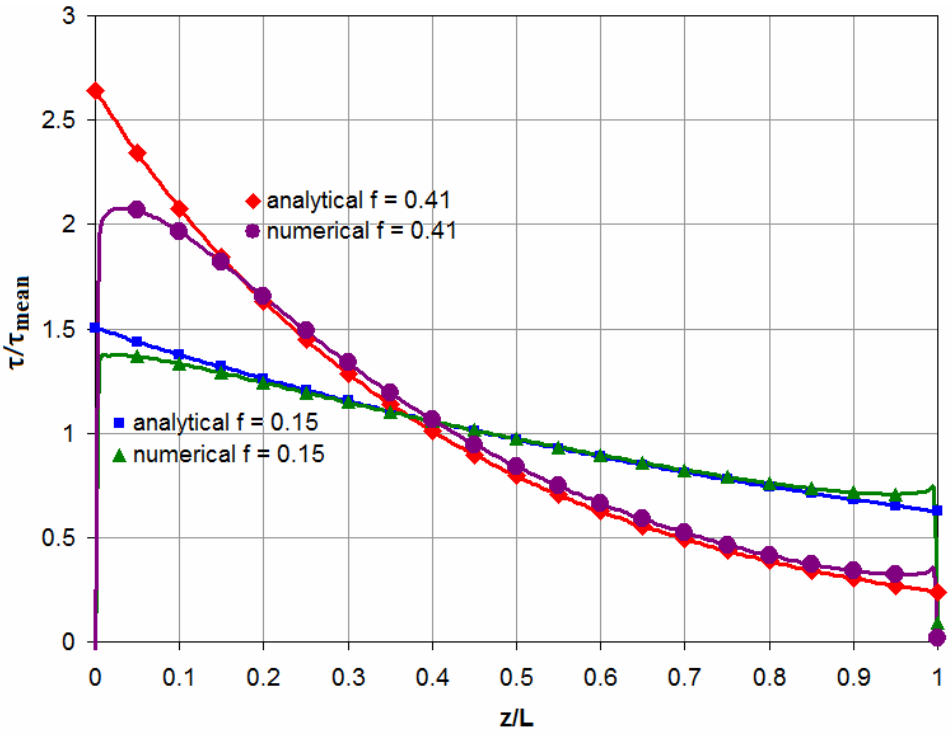

Figure 15: Numerical and analytical axial profiles of the friction stress for f = 0.15 and for f = 0.41.

4 Discussion of the assumptions and research findings

4.1 Verification of the elasticity assumption

In this section, we assume that the stresses are only generated by the tightening of the screw-nut system. Thus we can define $\varepsilon_{rr} = \varepsilon_{\theta\theta} = 0$. The invariants of the stress tensor (section 2.1) are thus formulated as follows:

$$P = \frac{1+\nu}{3\nu}\sigma_{rr}$$
$$\sigma_{eq} = \sqrt{\left(\frac{1-2\nu}{\nu}\sigma_{rr}\right)^2 + 3\sigma_{rz}{}^2} \quad (28)$$

The term $\sigma_{rz}{}^2$ is the highest at the contact with the tube (at $r = R$), the criterion defined by inequality (1) can therefore be reformulated by using the notations defined in relation (18):

$$\left[\sqrt{\left(\frac{1-2\nu}{\nu}\right)^2 + 3f^2} - \alpha\frac{1+\nu}{3\nu}\right]p < C \quad (29)$$

The condition (29) is verified whatever the p magnitude if:

$$f < \frac{\sqrt{\alpha^2(1+\nu)^2 - 9(1-2\nu)^2}}{3\nu\sqrt{3}} \quad (30)$$

In this particular case, this gives $f < 0.31$. The condition (29) is thus verified for the low-velocity tests for which $f = 0.15$.

For higher friction coefficients, the elasticity of the material is preserved if the pressure p remains under a certain value:

(31) $$p < \frac{C}{\sqrt{\left(\frac{1-2\nu}{\nu}\right)^2 + 3f^2} - \frac{\alpha(1+\nu)}{3\nu}}$$

For the high-velocity tests, it has been established that $f < 0.56$. $f = 0{,}56$ leads to the minimal value of $\frac{C}{\sqrt{\left(\frac{1-2\nu}{\nu}\right)^2 + 3f^2} - \frac{\alpha(1+\nu)}{3\nu}}$ and the corresponding maximal pressure p is 70 MPa.

According to relation (27), the maximal value of the stresses is 3.4 times higher than the value of the mean stress, which limits the mean pressure p_{mean} to around 20 MPa. Given the values reached by the mean pressures p_{mean} (Figure 14), the elasticity condition is respected.

4.2 Limits of the experimental device

Due to the fracture of the screw (which suddenly breaks in torsion) during its tightening, the pressure value of the device is limited to roughly 20 MPa and the compressed air gun used during the Hopkinson bar tests limits the possible range of relative velocity to roughly 5-20 m/s.

The proposed configuration merely gives macroscopic information on the interface conditions. It does not, therefore, enable less global information to be supplied on the sliding and namely on the transition between the sticking phase and the sliding phase.

As only the measurements of the friction force and of the external strain of the tube are available, a model is needed to estimate the friction coefficient and there are no overabundant measurements to confirm its adequacy.

5 Conclusion

The purpose of the study was to design an experimental configuration enabling the friction measurement between an inert material, mechanically representative of an explosive, and steel. The desired sliding velocities were of the order of 10 m/s and the desired pressures were several tens of MPa. A new confinement set-up was designed because of the low mechanical resistance of the material when submitted to the classical compression of commercial tribometers. The stresses and the friction coefficient between steel and the inert material have been identified from indirect measurements, from an analytical model and from numerical simulations of the mechanical response of the set-up.

The mean pressures reached almost 20 MPa whereas the classical pin-on-disk tribometer limits this pressure to 5 MPa [5]. The sliding velocities reached around 1 mm/min during low-velocity tests and around 10 m/s during high-velocity tests. An influence of the sliding velocity on the friction has been clearly demonstrated since the kinetic friction coefficient identified is around 0.15 for the low-velocity tests and of the order of 0.4-0.5 for the high-velocity tests.

These results are useful since there is otherwise very little data. Future researches should focus on:

- Understanding local behaviour (namely the onset of sliding), and in this objective there are ongoing developments to improve the metrology (measurement of fields) and analysis (inverse method) to obtain more localised data on the interface [19].
- Designing devices enabling the extension of the pressure range to 100 MPa and over. It has been done in [20] with a low-velocity tribometer which need to be adapted to high velocities.
- The achievement of higher velocities (100 m/s), for which another dynamic testing device would have to be designed.
- Modelling the friction process to understand the influence of the roughness [21], [22], [23] and the influence of the chemical interaction [24], [25], [26], [27].

Acknowledgements

The authors would like to thank the reviewers for their valuable comments.

6 References

[1]: Field J.E., Swallowe G.M., Heaven S.N., Ignition mechanisms of explosives during mechanical deformations, Proc Royal Society London A, 383 (1982), 231-44.

[2]: Chidester S.K., Green L.G., Lee C.G., A frictional work predictive method for the initiation of solid high explosives from low pressure impacts, Office National Research 333-95-12, Proc. 10th International Detonation Symposium, Boston (1993), p 786-792.

[3]: Vandersall K.S., Chidester S.K., Forbes J.W., Garcia F., Greenwood D.W., Switzer L.L and al., Experimental and modelling studies of crush, puncture, and perforation scenarios in the Steven impact test, In: Office Naval Research ONR 333-05-02, editors. Proc. 12th international detonation symposium; San Diego (2002), pp 131-139.

[4]: Kim W.S., Hector L.G., The Influence of Temporal Profile on Hyperbolic Heat Conduction in Materials Subjected to Repetitively Pulsed Laser Radiation, Mech. Res. Comm., 18(6) (1991), 419-428.

[5]: Dickson P.M., Parker G.R., Smilowitz L.B., Zucker J.M., Asay B.W., Frictional Heating and Ignition of Energetic Materials, CP845, Conference of the American Physical Society Topical Group on Shock Compression of Condensed Matter (2005), 1057-1060.

[6]: Hoffman, Chandler J.B., Aspect of the tribology of the plastic bonded explosive LX-04, Propellants, Explosives, Pyrotechnics, 29 (2004), 368-373.

[7]: Picart D., Delmaire-Sizes F., Gruau C., Trumel H., Ignition of HMX-based PBX submitted to impact: strain localization and boundary conditions, 16th Conference of the American Physical Society Topical Group on Shock Compression of Condensed Matter (2009).

[8]: Kim H.J., Emge A., Winter R.E., Keightley P.T., Kim W.K., Falk M.L., Rigney D.A., Nanostructures generated by explosively driven friction: Experiments and molecular dynamics simulations, Acta Materiala, 57 (2009), 5270-5282.

[9]: Prakash V., A pressure-shear plate impact experiment for investigating transient friction, Experimental Mechanics, 35(4) (1995), 329-336.

[10]: Rajagopalan S., Irfan M.A., Prakash V., Novel experimental techniques for investigating time resolved high speed friction, Wear, 225-229 (1999), 1222-1237.

[11]: Espinosa H.D., Patanella A., Fischer M., A Novel Dynamic Friction Experiment Using a modified Kolsky Bar Apparatus, Experimental Mechanics, 40(2) (2000), 138-153.

[12]: Huang H., Feng R., Dynamic Friction of SiC Surfaces: A Torsional Kolsky Bar Tribometer Study, Tribology Letters, 27 (2007), 329-338.

[13]: Rajagopalan, S. and Prakash V., A modified Kolsky bar for investigating dynamic friction. Experimental Mechanics, 39(4) (1999), 295-303.

[14]: Philippon S., Sutter G., Molinari A., An experimental study of friction at high sliding velocities, Wear, 257 (2004), 777-787.

[15]: Philippon S., Voyiadjis G.Z., Faure L., Lodygowski A., Rusinek A., Chevrier P., Dossou E., A Device Enhancement for the Dry Sliding Friction Coefficient Measurement Between Steel 1080 and VascoMax with Respect to Surface Roughness Changes, Experimental Mechanics, 51(3) (2011), 337-358.

[16]: Janssen H.A., Versuche über Getreiedruch in Silozellen, Vereins Z. Deutsch Eng., 39 (1895), 1045.

[17]: Bailly P., Delvare F., Vial J., Hanus J.L., Biessy M., Picart D., Dynamic behavior of an aggregate material at simultaneous high pressure and strain rate: SHPB triaxial tests, International Journal of Impact Engineering, 38 (2011), 73-84.

[18]: Forquin P., Safa K., Gary G., Influence of free water on the quasi-static and dynamic of strength of concrete in confined compression tests, Cement and Concrete Research, 40 (2009), 321-333.

[19]: Durand B., Delvare F., Bailly P., Numerical solution of Cauchy problems in linear elasticity in axisymmetric situations, International Journal of Solids and Structures, 48(21) (2011), 3041-3053.

[20]: Durand B., Delvare F., Bailly P., Picart D., Identification of the friction under high pressure between an aggregate material and steel: experimental and modelling aspects, International Journal of Solids and Structures, 50(24) (2013), 4108-4117.

[21]: Hector L.G. Jr., Sheu S., Focused Energy Beam Work Roll Surface Texturing Science and Technology, J. Materials Processing Manufacturing Science, 2(1) (1993), 63-117.

[22]: Hector L.G. Jr., Lippert K.B., Fridy J.M., Analysis of Engineering Surfaces, The Mathematica Journal, 6(2) (1996), 72-79.

[23]: Sheu S., Hector L.G. Jr., Tool Surface Morphologies for Friction and Wear Control in Metalworking Processes, ASME J. Tribology, 120 (1998), 517-527.

[24]: Adams J.B., Hector L.G. Jr., Siegel D.J., Yu H., Zhong J., Adhesion, Lubrication and Wear at the Atomic Scale, Surface and Interface Analysis, 31 (2001), 619-626.

[25]: Qi Y., Hector L.G., Adhesion and Adhesive Transfer at Aluminum/Diamond Interfaces: A First Principles Study, Phys. Rev., B. 69 (2004), 235401-1,13.

[26]: Zhang Q., Qi Y., Hector L.G. Jr., Cagin T., Goddard III W.A., Atomic Simulation of Kinetic Friction at Its Velocity Dependence at Al/Al and α-Al_2O_3/α-Al_2O_3 Interfaces, Phys. Rev., B. 72 (2005), 045406-1,12.

[27]: Zhang Q., Qi Y., Hector L.G. Jr., Cagin T., Goddard III W.A., Origin of Static Friction and its Relationship to Adhesion at the Atomic Scale, Phys. Rev., B. 75 (2007), 144114-1,7.